ADVANCED MATERIALS
www.advmat.de

Multimodal Digital X-ray Scanners with Synchronous Mapping of Tactile Pressure Distributions using Perovskites

Jiuk Jang, Sangyoon Ji, G. Krishnamurthy Grandhi, Han Bin Cho, Won Bin Im, and Jang-Ung Park**

Visual and tactile information are the key intuitive perceptions in sensory systems, and the synchronized detection of these two sensory modalities can enhance accuracy of object recognition by providing complementary information between them. Herein, multimodal integration of flexible, high-resolution X-ray detectors with a synchronous mapping of tactile pressure distributions for visualizing internal structures and morphologies of an object simultaneously is reported. As a visual-inspection method, perovskite materials that convert X-rays into charge carriers directly are synthesized. By incorporating pressure-sensitive air-dielectric transistors in the perovskite components, X-ray detectors with dual modalities (i.e., vision and touch) are attained as an active-matrix platform for digital visuotactile examinations. Also, in vivo X-ray imaging and pressure sensing are demonstrated using a live rat. This multiplexed platform has high spatial resolution and good flexibility, thereby providing highly accurate inspection and diagnoses even for the distorted images of nonplanar objects.

1. Introduction

Inspection of complex engineering systems and early diagnosis of diseases require the utilization of multiple sensor sources to acquire information.[1–6] Among the elements of the sensory systems, visual and tactile perceptions are the key intuitive parameters for object recognition,[7–9] and the synchronized detection of these two sensory modalities can enhance the accuracy of the cognitive system further by providing complementary information between them. For example, the multimodal interactions to combine visual and tactile sensing information take place in the human brain to maximize the object recognition performance.

As a visual-inspection method, X-ray detectors, which can examine the inside of the objects, have been implemented in various fields, such as industrial non-destructive testing, homeland security, and medical diagnostic imaging.[10–16] Although the X-ray inspection system is indispensable for the assessment of internal structures, which the human eye and optical cameras cannot observe, this X-ray inspection only provides visual information, which can limit the extension of its potential applications.[17] To improve the quality of inspection and diagnosis, the mapping of tactile pressure distributions should be used to detect excessive pressures, for example, the expansion of batteries before they explode and the fatigue failure of pipelines. Also, combining visual and tactile information makes it possible to diagnose various diseases (e.g., edema, scoliosis, and diabetes) by measuring additional pressure-related factors, such as body pressure and the circulation of blood, which cannot be measured by X-ray radiography alone.[18–20] Therefore, using a multimodal sensory platform that consists of X-ray detectors and tactile pressure sensors, which allows the simultaneous visuotactile imaging of the internal structures and external morphologies of target objects, can be an effective way to acquire accurate inspections.

Metal halide perovskites are a new generation of semiconductor materials with extraordinary properties that allow the direct conversion of X-rays into electronic signals. Although these perovskites can be fabricated using a low-temperature solution process, their 3D integration capability for multiplexed sensory platforms has been limited due to their inherent vulnerability to the heat and moisture in the fabrication process, both of which degrade their remarkable optoelectronic properties.[21] Recently, direct-conversion X-ray detectors have been reported in which the perovskite layer is simply coated onto a commercially available Si transistor array for digitized pixel imaging.[14] However, the rigid and fragile form of this Si transistor

Dr. J. Jang, Dr. S. Ji, Prof. J.-U. Park
Nano Science Technology Institute
Department of Materials Science and Engineering
Yonsei University
Seoul 03722, Republic of Korea
E-mail: jang-ung@yonsei.ac.kr
Dr. G. K. Grandhi, H. B. Cho, Prof. W. B. Im
Division of Materials Science and Engineering
Hanyang University
Seoul 04763, Republic of Korea
E-mail: imwonbin@hanyang.ac.kr
The ORCID identification number(s) for the author(s) of this article can be found under https://doi.org/10.1002/adma.202008539.

DOI: 10.1002/adma.202008539

backplane prevents the X-ray detectors to be fabricated in a flexible form, with still providing only visual information of the target.[22–27] To our knowledge, flexible and multimodal sensory platforms for simultaneous visuotactile imaging have not been examined despite their great potential for better quality inspections of non-flat objects in medicine, industry, and security.

Herein, we demonstrate multimodal integration of flexible, high-resolution X-ray detectors with a synchronous mapping of tactile pressure distributions, as a visuotactile sensory platform with an active-matrix form, to obtain digital images of internal structures and morphologies simultaneously. The development of this multiplexed sensory platform includes several unique strategies as follows. First, as an X-ray-sensitive layer, we synthesize guanidinium (GA, $C(NH_2)_3^+$)-doped methylammonium lead triiodide ($MAPbI_3$, where MA = $CH_3NH_2^+$), which can convert X-rays directly into charge carriers, by substituting the MA molecules of $MAPbI_3$ into GA molecules to enhance their environmental stability and optoelectronic properties. This GA-doped $MAPbI_3$ presents a high X-ray sensitivity of 6.74 μC mGy_{air} cm^{-2} with an X-ray tube voltage of 50 kV, which is at least one order of magnitude higher than that of X-ray detectors based on commercial amorphous selenium (α-Se, 0.5 μC mGy_{air} cm^{-2}) or thallium-doped cesium iodide (CsI:Tl, 0.38 μC mGy_{air} cm^{-2}).[28,29] Also, this GA-doped $MAPbI_3$ exhibits outstanding stability over a year at ambient conditions. Second, we implement an active-matrix array of pressure-sensitive indium gallium zinc oxide (IGZO) thin film transistors (TFTs) with air-dielectric layers. These top-gated TFTs with local air gaps as dielectrics present negligible hysteresis, which is advantageous to their rapid response time due to the clean interface between the IGZO channel and the air-dielectric layer. The height of the air-dielectric layer is determined by the thickness of the elastomeric partition spacers between IGZO and the top-gate, and the height is decreased by applying tactile pressure to increase the capacitance of the gate–air–IGZO structure. This pressure-sensitive change in capacitance enables an individual TFT to act solely as a single pressure sensor. Third, we integrate each pressure-sensitive, air-dielectric TFT with the perovskite layer (i.e., GA-doped $MAPbI_3$) to form a 3D active-matrix structure of their array, thereby achieving a multimodal X-ray scanner with synchronous mapping of tactile pressures for digital visuotactile analysis. Because the air-dielectric TFTs operate as an active-matrix backplane as well as pressure sensors, this multiplexed platform can be fabricated without additional components, such as photodiodes or pressure-sensitive rubbers; therefore, high spatial resolutions can be achieved (pixel pitch of 50 μm). Also, we demonstrate the simultaneous in vivo imaging of the anatomical structure and the pressure distribution of the rat's foot using this multiplexed platform, thereby indicating the substantial potential of this multimodal system for next-generation non-destructive examinations and medical diagnoses.

2. Result and Discussions

Recently, Pb-based perovskite materials have been explored for the detection of high-energy ionizing photons, including X-rays and gamma-rays (γ-rays). $MAPbI_3$, which has a high charge carrier lifetime and diffusion lengths in a single-crystal, has been developed in solution-processable form, allowing polycrystalline $MAPbI_3$ to be used in the integration of flexible electronics.[30] Because it has issues concerning stability, numerous efforts have been made to synthesize solution-processed, stable-state $MAPbI_3$. Among these efforts, the mixed A-cation approach has been considered as an efficient way to stabilize perovskite films, and GA is an interesting candidate as an A-type organic cation for $APbX_3$-type perovskites, which has produced highly efficient perovskite solar cells.[31–35] In this work, we utilized GA-doped solution-processed $MAPbI_3$ films for the X-ray sensitive layer. **Figure 1**a shows the variation of the tolerance factor of $GA_xMA_{1-x}PbI_3$ as a function of the concentration of GA. This factor increases in proportion to the concentration of GA, and it approaches 1 when ≈70% of the MA has been replaced by GA, indicating that the incorporation of GA can enhance the stability of perovskite films. Even so, the pure $GA_xMA_{1-x}PbI_3$ phase without the $GAPbI_3$ impurity (secondary) phase was obtained only when the GA that was incorporated was less than 25%, as indicated by the red-dashed line in Figure 1a.[33] The difference in the number of hydrogen bonds between MA and GA causes the GA-induced enhanced stability of $MAPbI_3$. One GA molecule (six hydrogen atoms) can form six hydrogen bonds with neighboring iodides compared to two hydrogen bonds by an MA molecule and strengthen the host lattice. This, in turn, increases negative formation enthalpy and hence the stability of $MAPbI_3$ upon GA incorporation, as revealed by density functional theory calculations.[33] Lead halide perovskites fulfill the criteria for X-ray detection. Heavy elements-containing perovskites absorb high energy radiation efficiently. This is because X-ray absorption is proportional to Z^4/E^3, where Z and E are atomic number and energy of radiation, respectively. Figure S1, Supporting Information, compares absorption of the perovskite material and the state-of-the-art X-ray detection material (α-Se) at photon energies between 10 keV and 1 MeV. The perovskite outperforms α-Se at most of the photon energies. A path length (thickness) of a few hundreds of micrometers to a few millimeters is desirable for X-ray attenuation. A very low trap density and high charge-carrier mobility–lifetime ($\mu\tau$) product, of $MAPbI_3$-based films (≈10^{-4} cm^2 V^{-1}),[14] facilitates an efficient charge collection at the electrodes. As shown in Figure 1b, it is evident that MA possesses a non-zero dipole moment, whereas GA is a planar molecule with a zero-dipole moment. The faster reorientation rates of A-site cations (e.g., GA) in the mixed-cation perovskites (e.g., $MAPbI_3$) result in slower charge recombination (i.e., longer charge carrier lifetime) and hence higher $\mu\tau$ product, which is favorable for a large photocurrents.[34,36,37] Also, it was found that 10% replacement of MA in $MAPbI_3$ with GA leads to the longest radiative recombination time among the GA concentrations (0% < GA < 25%).[34] This suggests that the incorporation of GA can improve the performance and the stability of $MAPbI_3$-based X-ray detectors. Additionally, the large bulk resistivity (≈10^7 Ω cm) of the $MAPbI_3$-based films ensures a low limit of detection (LOD) by reducing dark current and noise.[38] As shown in Figure 1c, the scanning electron microscopy (SEM) images of the as-obtained GA-doped $MAPbI_3$ films exhibit uniform morphology with microscale grain (5–10 μm), and these large grain sizes have been predicted to improve the

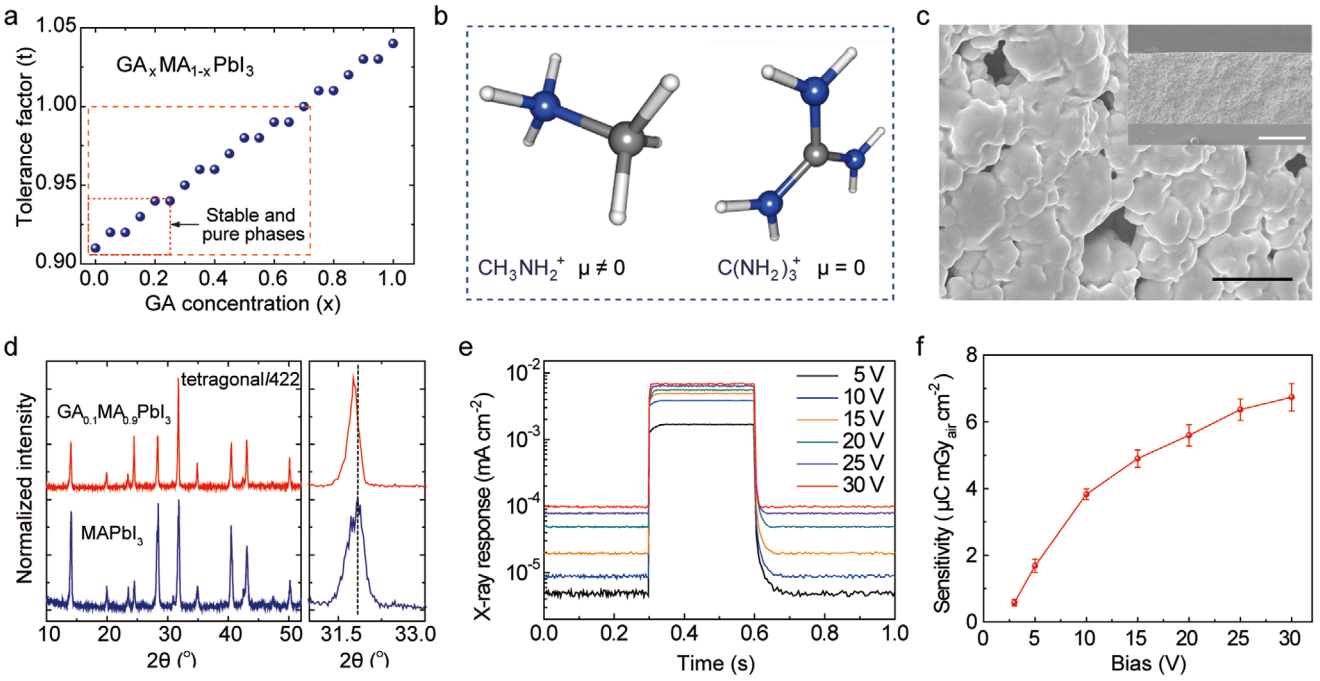

Figure 1. Synthesis and characterizations of GA-doped $MAPbI_3$. a) The tolerance factor of $GA_xMA_{1-x}PbI_3$ as a function of GA concentration. b) The molecular structures of MA and GA along with their net dipole moments (μ). The blue, gray, and white colored spheres represent nitrogen, carbon, and hydrogen, respectively. c) The SEM image of $GA_{0.1}MA_{0.9}PbI_3$ film showing micrometer-sized grains. Scale bar: 50 μm. The inset shows the cross-sectional SEM image of the film. Scale bar: 200 μm. d) The XRD spectra of pure $MAPbI_3$ and $GA_{0.1}MA_{0.9}PbI_3$ films. e) Real-time response of the diode-configured X-ray detector under X-ray irradiation (tube voltage of 50 kV, and dose rate of 1.6 mGy_{air} s^{-1} for 300 ms) with varying applied bias voltage. f) The sensitivities of the X-ray detector as a function of bias voltage.

performance of X-ray detectors.[14] The thickness of the film was 300 μm, which is sufficient to absorb most of the X-ray photons below 50 keV. Figure 1d shows the X-ray diffraction (XRD) results of the $GA_{0.1}MA_{0.9}PbI_3$ film, which was crystallized in the tetragonal phase. The small shift toward a lower diffraction angle in the GA-doped $MAPbI_3$ film compared to pure $MAPbI_3$ implied the incorporation of larger GA cations into the $MAPbI_3$ lattice. Also, the GA-doped $MAPbI_3$ film exhibited long-term stability (Figure S2, Supporting Information). As shown in the XRD pattern of the $GA_{0.1}MA_{0.9}PbI_3$ film, which was stored in the ambient conditions (25 °C, 20% of relative humidity) for a year, the film remained stable for an extended period of time. The long-term stability of $GA_{0.1}MA_{0.9}PbI_3$ film is consistent with a literature report.[39] The same literature report demonstrates that further incorporation of GA (15%) leads to the appearance of PbI_2 and GA from $GA_{0.15}MA_{0.85}PbI_3$ film after 8 months of storage. Hence, ≤10% GA incorporation is probably optimal for achieving the desired long-term stability for $GA_xMA_{1-x}PbI_3$ films. As a result of both improved charge carrier recombination time and long-term stability, we replaced 10% of MA in $MAPbI_3$ with GA in order to fabricate a stable X-ray detector.

To characterize the X-ray response of the GA-doped $MAPbI_3$ film, we fabricated diode-configured X-ray detectors that consisted of an indium tin oxide (ITO) electrode, poly(3,4-ethylene dioxythiophene) polystyrene sulfonate (PEDOT:PSS), and titanium dioxide nanopowder (TiO_2) (Figure S3, Supporting Information). The detailed fabrication methods are provided in the Supporting Information's Methods section. Figure 1e shows the electrical response of this diode-configured X-ray detector during the irradiation of the X-ray with a tube voltage of 50 kV and a dose rate of 1.6 mGy_{air} s^{-1} for 300 ms. Electrical fields ranging from 5 to 30 V (0.017–0.1 V μm^{-1}) were applied to collect charges through the bottom ITO electrode. Figure 1f shows that an X-ray sensitivity of 6.74 μC mGy_{air} cm^{-2} was achieved at 0.1 V μm^{-1}, which was at least one order of magnitude higher than that of X-ray detectors based on commercial amorphous selenium (α-Se, 0.5 μC mGy_{air} cm^{-2}) or thallium-doped cesium iodide (CsI:Tl, 0.38 μC mGy_{air} cm^{-2}).[28,29] Also, both response and recovery times were decreased as the bias was increased from 5 to 30 V, as shown in Figure S4, Supporting Information. In case of a bias of 30 V, the response time and recovery time were 10 and 13 ms, respectively.

Figure 2a shows schematic illustrations of the multiplexed detector that is capable of the simultaneous mapping of X-ray radiation and the distribution of the tactile pressure. The multiplexed detector consists of the GA-doped $MAPbI_3$ layer for the direct conversion of X-rays into charge carriers and IGZO TFT arrays for sensing pressure and processing data. When the multiplexed detector is exposed to X-ray radiation, the charge carriers generated in the perovskite layer can be collected through the charge collection electrodes connected to the drain contact pads of each TFT pixel, and, therefore, the intensity of the X-rays can be quantified by measuring the drain current (I_D) of the TFT arrays. For the synchronous detection of pressure, elastomeric partition spacers were formed between the IGZO channel and the top-gate electrode. The capacitance of the metal-air-IGZO depends on the pressure-induced thickness

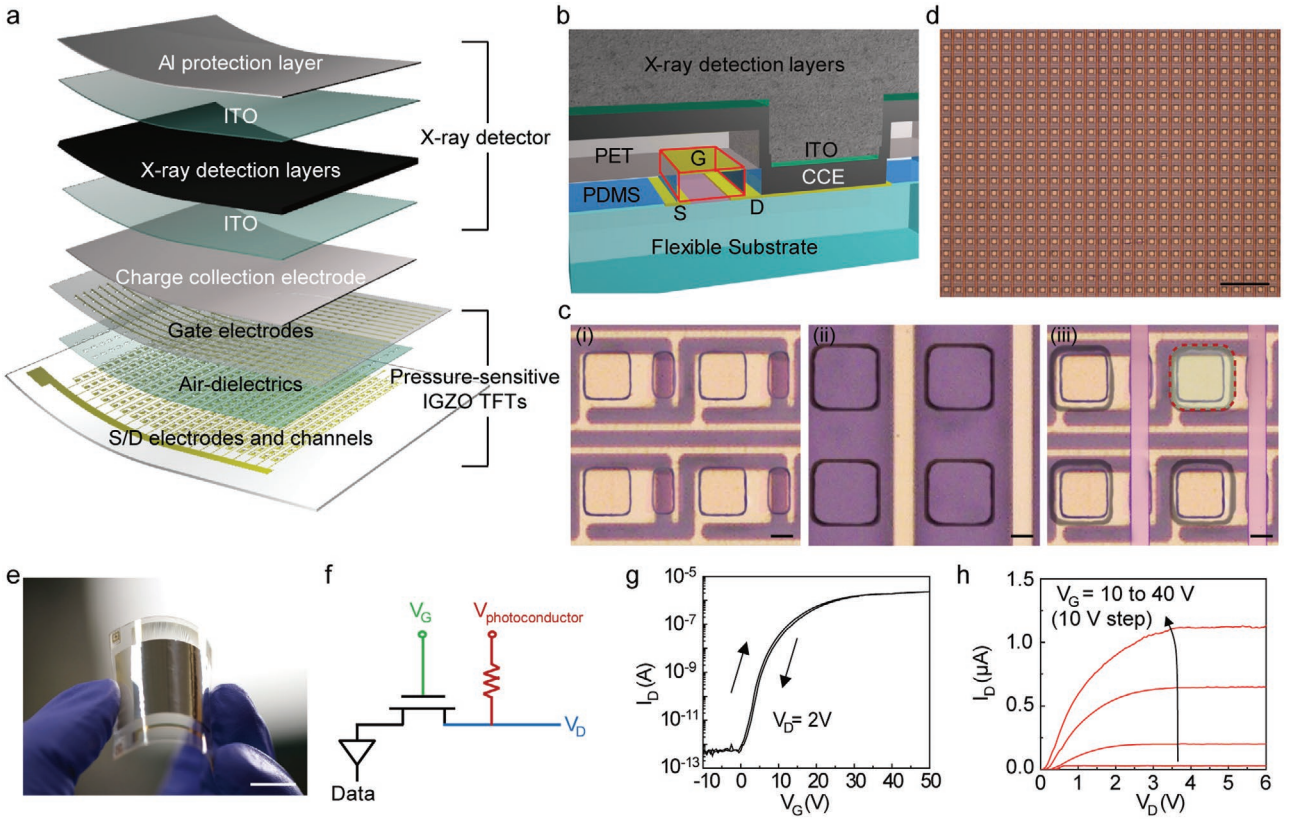

Figure 2. Integration of the pressure-sensitive IGZO TFT arrays with the perovskite layer. a) Schematic layouts of the multiplexed detector that consisted of pressure-sensitive IGZO TFTs and X-ray detectors. b) Schematic image of the cross-sectional perspective view of the fully-integrated multiplexed detector. c) Optical microscopy images before the integration of the perovskite layers. The bottom panel consists of the IGZO channels, S/D electrodes, and elastomeric partition spacers with via holes (i). The top panel consists of the gate electrode and via holes (ii). The bottom and top panel are integrated with the alignment of via holes (iii). Scale bars: 10 μm. d) Optical microscopy image of a high-resolution pressure-sensitive IGZO TFT arrays with a pixel pitch of 50 μm. Scale bar: 200 μm. e) Photograph of a flexible, high-resolution multiplexed detector with a sensing area of 2 × 2 cm. Scale bar: 1 cm. f) Circuit diagram of the multiplexed detector. g,h) Transfer characteristic (V_D = 2 V) and output characteristic (V_G = 10 to 40 V) of the multiplexed detector.

modulation of the air-dielectric layer, and this pressure-sensitive change in capacitance allows the individual IGZO TFT to act solely as a single pressure sensor (Figure 2b). The detailed method of the fabrication process is provided in Figure S5, Supporting Information. Figure 2c shows optical microscopy images of individual TFT pixels according to the steps in the fabrication process. As a channel material, we utilized a representative oxide semiconductor material, that is, amorphous IGZO, due to its flexibility, high mobility, and less leakage current in the amorphous states.[40] The thin-film IGZO was deposited on the 25-μm-thick polyimide (PI) film with a thickness of 20 nm at 200 °C by radio frequency magnetron sputtering, and it was photolithographically patterned as a channel. The width and the length of the IGZO channel were 16 and 6 μm, respectively. As a source (S) and drain (D) electrode, Al and Au were deposited (20 nm of Al and 60 nm of Au) by thermal evaporation and patterned photolithography. For the elastomeric partition spacer, poly(dimethylsiloxane) (PDMS) film (thickness of 35 μm) was cut by a laser ablation system (CO_2 laser, Epilog Mini 18, Cutting Edge Systems, Inc.) to make two holes for connecting the perovskite and drain electrodes and for defining the local air gap as the dielectrics (Figure 2c-i).[41–43] The gate electrode (G) was formed by thermal evaporation of Cr/Au (5 nm/60 nm) and photolithography on the other panel of a 25-μm-thick PI film. Then, via holes were formed by a CO_2 laser at the same positions as those of the PDMS layer (Figure 2c-ii). Subsequently, this panel was laminated onto the bottom panel (Figure 2c-iii) by defining the charge collection areas with dimensions of 25 × 25 μm. For precise alignment of each layer, we used a stage that could be moved in the *x*, *y*, and *z* axes and an optical microscope.[44] Figure 2d shows an optical microscopy image of the high-resolution, pressure-sensitive IGZO TFT arrays with a pixel pitch of 50 μm. This pixel pitch was similar to the pixel pitch of a commercial digital X-ray detector, suggesting that these IGZO TFT arrays can be utilized as a backplane for the multiplexed X-ray detector with high spatial resolution. Also, this active-matrix array of TFTs can minimize the interference between adjacent pixels by switching every pixel sequentially, thereby reducing the crosstalk for X-ray detection.

Prior to the integration of the X-ray detection layers and the IGZO TFT backplane, a liquid metal of an eutectic gallium–indium alloy (EGaIn), which is a stretchable via interconnect material, was deposited using a doctor blade coating

for the electrical connection between the perovskite and drain electrode of TFT. The X-ray detection layers, including the Al protective layer, were formed on the TFT backplane with the same structure as described in Figure 1 and in the Experimental Section. Figure 2e shows a photograph of a multiplexed detector with a sensing area of 2 × 2 cm, that is, 4 cm^2. The sensing mechanism of the multiplexed detector is described in the circuit diagram of Figure 2f. For simultaneous detection of X-ray and tactile pressures, the DC bias to operate the X-ray detector was applied to the terminal of $V_{photoconductor}$ in addition to the gate voltage (V_G) and drain voltage (V_D) for the operation of IGZO TFT. Since the photocurrent induced by the GA-doped $MAPbI_3$ layer was negligible in the dark state, the I_D of the IGZO TFT was changed only by modulating the thickness of air-dielectric layer, that is, the applied pressure. When the multiplexed detector was exposed to the X-rays, the I_D of the IGZO TFT increased due to the additional photocurrent generated in the photoconductor. Using this mechanism, the X-rays and the pressure can be detected simultaneously. Figure 2g,h show the transfer and output characteristics of the IGZO TFT ($V_{photoconductor}$ = 30 V). The n-channel mobility and on/off ratio of I_D ($I_{on/off}$) of this TFT were calculated to be ≈12 $cm^2\ V^{-1}\ s^{-1}$ and 4.0 × 10^6, respectively, with the threshold voltages (V_{th}) of 11 V. This mobility, which originated from the clean interfaces between the IGZO and air, was sufficiently high compared to that of the a-Si transistors used for commercial LCD and OLED displays (≈1 $cm^2\ V^{-1}\ s^{-1}$).[42] The statistical distributions of the field-effect mobilities of the 500 TFTs are provided in Figure S6, Supporting Information, and these data follow Gaussian profiles. Also, Figure S7, Supporting Information, shows the statistical distributions of the field-effect mobility, $I_{on/off}$, and V_{th} of 16 000 TFTs. They were calculated as 12.0 (± 1.9) $cm^2\ V^{-1}\ s^{-1}$, 4.0 × 10^6 (±1.9 × 10^6), and 10.8 (± 0.6) V, respectively, suggesting the good reproducibility of the TFT arrays.

To evaluate the pressure sensing characteristics, a well-defined load was applied and measured using an experimental setup that consisted of a motorized *z*-axis stage (Mark-10 ESM303) and a force gauge (Mark-10 M7-20) (Figure S8, Supporting Information). For the operation of the multiplexed detector, we applied biases of 30, 2, and 30 V to the terminals of V_G, V_D, and $V_{photoconductor}$, respectively. **Figure 3**a shows the real-time detection of relative changes in I_D ($\Delta I_D/I_0$, where I_0 is the current at zero Pascal with dark state, and $\Delta I_D = I - I_0$) when the pressure was applied stepwise over the range from 5 to 400 kPa without X-ray irradiation. As shown in the graph, the magnitudes of the pressures were distinguished clearly as step-like features, and it showed relatively fast response (20 ms) and recovery times (28 ms) with negligible hysteresis (Figure 3b). The response time and recovery time indicate the time to reach 95% and 5% of the saturated $\Delta I_D/I_0$ value, respectively. The changes in the thickness of the air-dielectric layer (i.e., the thickness of PDMS) and the modulation of I_D due to the applied pressure were well matched, thereby providing their qualitative dependency to the applied pressures (Figure 3c). Also, sensitivity to the applied pressure (*P*), which is defined as $(\Delta I_D/I_0)/P$, was calculated from the linear fit of the plot. In the pressure range of 0–400 kPa, the electrical signal of the multiplexed detector exhibited a sensitivity of 1.16 MPa^{-1} with high linearity. Because of the superior mechanical durability of the PDMS layer, the multiplexed detector showed excellent reliability during repetitive applications of a pressure of 400 kPa for 100 cycles (Figure 3d).

To investigate the optoelectronic properties of the multiplexed detector, we exposed X-rays without applying pressure, and the voltage of the X-ray tube was kept at 50 kV during the measurements. Figure 3e shows the real-time I_D measurement of the multiplexed detector during irradiation by X-rays at different dose rates. The $\Delta I_D/I_0$ increased as the X-ray dose rate increased from 0.2 to 3.1 $mGy_{air}\ s^{-1}$ with a linear dependency, suggesting that this multiplexed detector can be used for medical radiography that requires low dosage, such as mammography (0.4 mGy). Figure 3f shows that the multiplexed detector had a fast response time (13 ms) and recovery time (17 ms) when exposed to X-ray irradiation (1.6 $mGy_{air}\ s^{-1}$) with negligible hysteresis. The photostability of the multiplexed detector was analyzed by measuring $\Delta I_D/I_0$ during continuous or repeated X-ray irradiation (1.6 $mGy_{air}\ s^{-1}$) (Figure 3g). The $\Delta I_D/I_0$ of the multiplexed detector was negligible even after repetitive X-ray irradiation of 45 cycles and continuous X-ray irradiation for 900 s, thereby providing excellent photostability which is advantageous for practical applications. Figure S9, Supporting Information, exhibits the long-term photostability of the perovskite. The $\Delta I_D/I_0$ changed only 8.6% of its original value during the 2000 cycles of the repetitive X-ray irradiation, suggesting the good stability of this perovskite material with the GA incorporation.[39] In addition, the relative changes in sensitivities ($\Delta S_D/S_0$) of the multiplexed detector (total thickness of ≈380 μm) with different radii of bending curvatures (R_c) were measured to determine the mechanical stability. For the bending test, the multiplexed detector was fixed to the half-cylindrical support with various radii of bending curvature, as shown in Figure 3h. As plotted in Figure 3i, the X-ray and pressure sensitivities of the multiplexed detector decreased only slightly with the R_c of 1 cm. Also, the long-term mechanical stability was analyzed by measuring $\Delta I_D/I_0$ during the repetitive applications of pressure (Figure S10a, Supporting Information) and bending (Figure S10b, Supporting Information). The $\Delta I_D/I_0$ changed negligibly after 2000 cycles of these repetitive applications, suggesting that the good mechanical stability of this device. Using this multiplexed detector, we performed real-time imaging of the internal structure of the electronic circuit was imaged by utilizing the X-ray detecting capability. Figure S11, Supporting Information, presents an X-ray image of the printed circuit board that corresponds to the area indicated by the white box in the photograph (50 kV and 1.6 $mGy_{air}\ s^{-1}$ for 500 ms). Since the sensing area of the multiplexed detector was 2 × 2 cm, the area corresponding to the white box (4 × 4 cm) was divided into four sections and imaged separately, and they were combined later to make a complete image.

To characterize the multiplexed detector with two sensory modalities (i.e., vision and touch), we demonstrated simultaneous imaging of the anatomical structure and the pressure distribution in the foot of a live rat. Because the feet can indicate underlying health conditions, combining the external

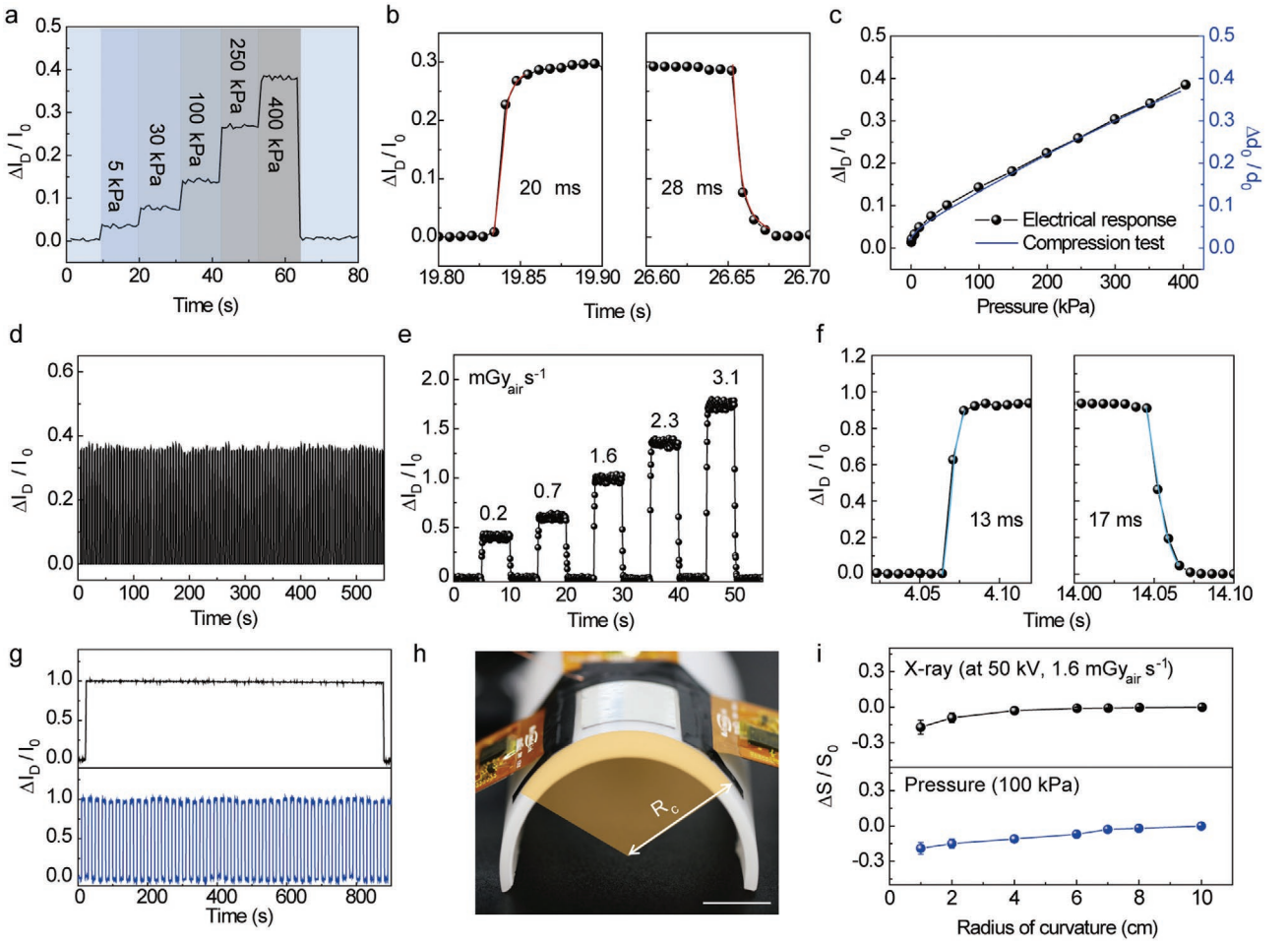

Figure 3. Characteristics of the sensors in the multiplexed detector for tactile pressures and X-rays. a) Real-time detection of the $\Delta I_D/I_0$ when the pressure was applied stepwise ranging from 5 to 400 kPa without X-ray irradiation (the biases of 30, 2, and 30 V were applied to the terminals of the V_G, V_D, and $V_{photoconductor}$, respectively). b) Response and recovery time of the multiplexed detector with the applied pressure of 250 kPa. c) Comparison between electrical response of the multiplexed detector under applied pressure and true strain–stress curve from the compression test of PDMS. d) Reliability of the multiplexed detector during the repetitive application of 100 cycles at a pressure of 400 kPa. e) Real-time detection of the $\Delta I_D/I_0$ during X-ray irradiation with different dose rates from 0.2 to 3.1 $mGy_{air}\ s^{-1}$ ($V_{photoconductor}$ = 30 V). The voltage of the X-ray tube was kept at 50 kV. f) Response and recovery time of the multiplexed detector with the X-ray dose rate of 1.6 $mGy_{air}\ s^{-1}$. g) Photostability of the multiplexed detector during the continuous (top) or repetitive (bottom) X-ray irradiation (1.6 $mGy_{air}\ s^{-1}$). h) Photograph of the experimental setup for the bending test. Scale bar: 1 cm. i) Relative changes in sensitivities ($\Delta S_D/S_0$) of the multiplexed detector for each physical quantity (i.e., X-ray and tactile pressure) with different radii of bending curvatures.

(e.g., pressure distribution and morphological characteristics) and internal (e.g., tissue damage and fracture) information of the feet can provide the comprehensive health status of the entire body as well as the feet.[45] **Figure 4**a shows an experimental set-up (left) for in vivo X-ray radiography and pressure distribution imaging of the foot and an enlarged image of the rat's foot (right). Because this multiplexed detector acquires data for two different physical quantities with the same readouts (i.e., I_D) using a single TFT, it requires a simple calibration process to distinguish each signal. Figure 4b shows the calibration steps, that is, i) the pressure distribution is mapped spatially by measuring the $\Delta I_D/I_0$ ($I_D = I_{Pressure}$) without the X-ray irradiation; ii) when the X-ray is irradiated, the photocurrent due to the charge carrier generated in the perovskite layer increases the $\Delta I_D/I_0$ ($I_D = I_{Pressure} + I_{photoconductor}$) of the multiplexed detector; iii) by subtracting the current corresponding to step (i) from the current of step (ii), only the $\Delta I_D/I_0$ ($I_D = I_{photoconductor}$) by X-ray can be extracted. The contour plots of the resultant signals, that is, ($\Delta I_D/I_0$) of step (i) and (iii), present the contour plots of the pressure distribution and X-ray radiography, respectively. The graphs in Figure 4c show the normalized signals measured along the dotted lines shown in Figure 4b. Through the calibration process, the clear signals of the pressure distribution (i) and X-ray radiography (iii) can be obtained. Figure 4d,e, respectively, show contour plots of the distribution of the pressure and the anatomical structure of the rat's foot, which are mapped simultaneously by the multiplexed detector with a calibration process. Movie S1, Supporting Information, shows the real-time in vivo mapping of the X-ray and the pressure. The measured value for each

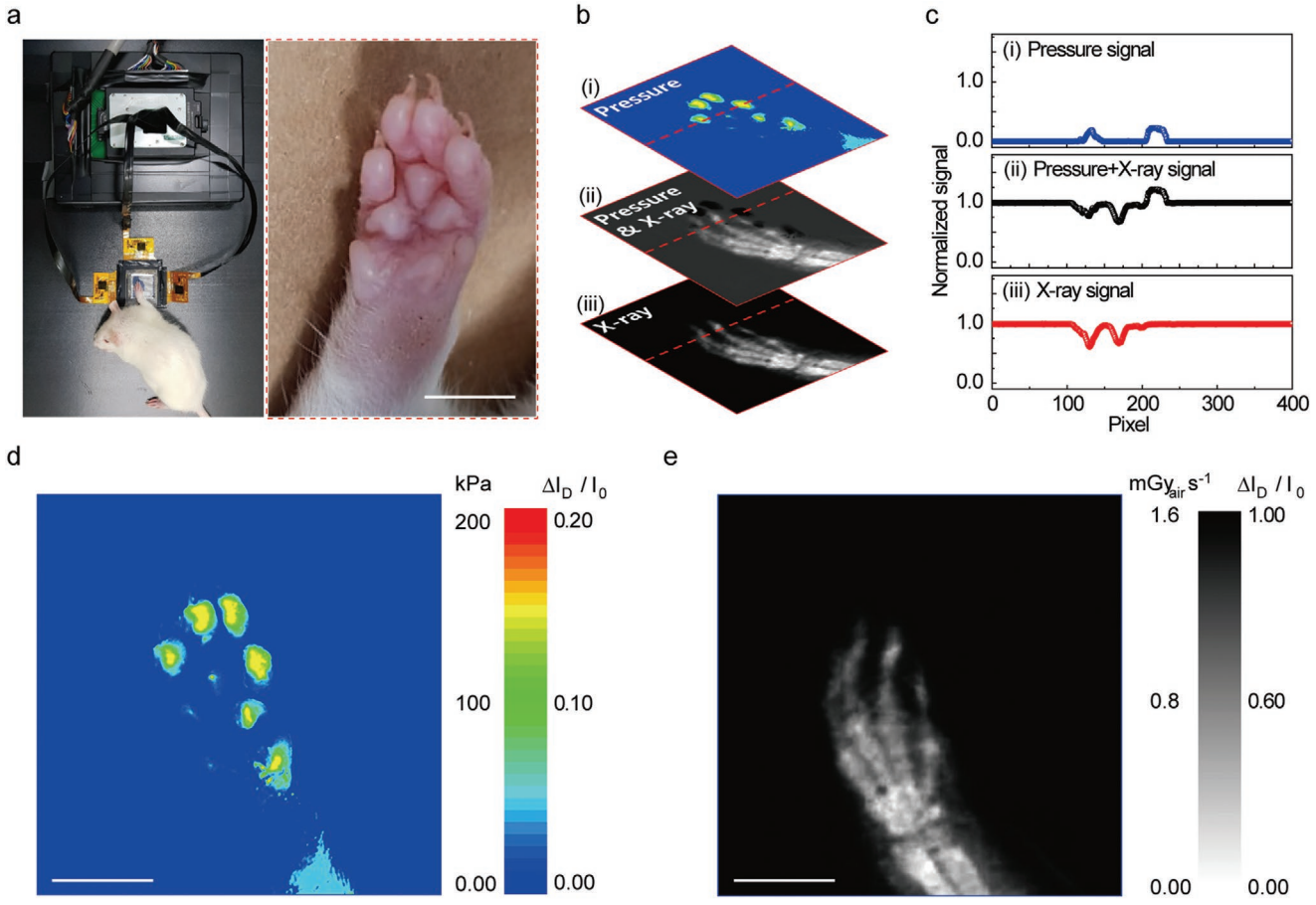

Figure 4. In vivo imaging of the X-ray and the pressure. a) Photographs of the experimental set-up (left) for in vivo radiography and pressure distribution imaging of the foot and an enlarged image of the rat's foot (right). Scale bar: 5 mm. b) Calibration process to distinguish the complex signals from visual (i.e., X-rays) and tactile (i.e., pressure) information. i,iii) Contour plot of the pressure distribution, and X-ray radiography, respectively. c) Normalized $\Delta I_D/I_0$ measured along the red dotted line in the contour plots in (b). d,e) Contour plots of the pressure distribution and anatomical structure of the rat's foot obtained by the multiplexed detector after the calibration process. The voltage of the X-ray tube was kept at 50 kV with a dose rate of 1.6 mGy_{air} s^{-1} for 500 ms (total X-ray dose: 0.8 mGy_{air}). Scale bars: 5 mm.

physical quantity (i.e., pressure or X-ray) can be controlled by adjusting the measurement conditions (i.e., V_G and $V_{photoconductor}$). Figure S12, Supporting Information, provides the distribution of $\Delta I_D/I_0$ ($I_D = I_{Pressure} + I_{photoconductor}$) according to the voltage bias condition, which suggests that this multiplexed detector can emphasize or eliminate each signal with respect to the target applications. As a standard for measuring the spatial resolution of the X-ray detector, we utilized the image quality indicator with paired wire (IQI, duplex IQI, EN 462–5), which consists of 13 conditions (Figure S13 and Table S1, Supporting Information). After X-ray imaging of the duplex IQI sample (50 kV and 1.6 mGy_{air} s^{-1} for 500 ms), the average of the peaks that correspond to the two lines of paired wire was evaluated mathematically using a line profile tool. In general, a dip between the wires should exceed 20% of the signal to be determined as spatially distinguished.[46] As shown in Figure S14, Supporting Information, an image of 10D (diameter and spacing of 100 µm) exhibited a dip value of 25.7%, whereas that of 11D had a dip value of 7.1%, suggesting that the multiplexed detector can distinguish between two adjacent objects that are only 100 µm apart.

3. Conclusion

As a visuotactile sensory platform with an active-matrix form, we developed flexible, high-resolution X-ray detectors with a synchronous mapping of tactile pressure distributions that can provide internal and external information of target objects as digital images in real time. For this purpose, we synthesized the GA-doped $MAPbI_3$ perovskite, which can convert X-rays directly into charge carriers to enhance the environmental stability and the optoelectronic properties. Also, by incorporating an active-matrix array of pressure-sensitive air-dielectric TFTs into this perovskite layer, the multiplexed visuotactile sensory platform for the simultaneous detections of X-rays and pressures was realized with its flexible form. This multiplexed digital scanner with two sensory modalities (i.e., X-ray vision and touch) presents high spatial resolutions and good flexibility, thereby providing high accuracy of the inspection and diagnosis even for the distorted images of nonplanar objects. As an example, we demonstrated simultaneous in vivo imaging of the tactile pressure distribution and X-ray radiography using the foot of a live rat. We expect, in fact, that exploration of various

applications in non-destructive industrial testing and medical diagnosis (such as the expansion of batteries and the fatigue failure of pipelines, as well as the diagnosis of edema, scoliosis, and other pressure-related diseases, represents promising areas for future work.

4. Experimental Section

Synthesis of the $GA_{0.1}MA_{0.9}PbI_3$ Perovskite Film: Lead iodide (PbI_2), methylammonium iodide (MAI), guanidinium iodide (GAI), α-terpineol, and γ-butyrolactone were purchased from Sigma-Aldrich and were used without any further purification. The blade-coating technique was employed to obtain perovskite films. The GA-doped $MAPbI_3$ paste was obtained by using both solvent (γ-butyrolactone) and antisolvent (α-terpineol). A mixture of MAI, GAI, PbI_2 were taken in a closed bottle in the desired molar ratio along with white ceramic balls. 78 wt% of iodide precursors in total were mixed with 22 wt% of γ-butyrolactone, and 40 wt% of α-terpineol with respect to γ-butyrolactone was mixed. The bottle was mounted on a ball mill, and the milling continued until a clear and dense black color perovskite paste was obtained. This viscous perovskite paste could be readily printed using a doctor blade. The thickness of the films was controlled by changing the height of the blade. The as-coated films were cured on a hot plate at 120 °C for 2 h to obtain $GA_{0.1}MA_{0.9}PbI_3$ films. Pure $MAPbI_3$ films were obtained by following the same procedure; however, GAI is not added.

Integration of the Pressure-Sensitive IGZO TFT Backplane with the Perovskite Layer: Prior to the integration of the X-ray detection layers and as-prepared IGZO TFT backplane, liquid metal (EGaIn), a stretchable and electrical via interconnect, was deposited using doctor blade coating with a thickness of 25 µm for electrical connection between perovskite and drain contact pads. The X-ray detection layers including Al protection layer were formed on the TFT backplane by same structure and method with a single-pixel diode.

Characterization of Pressure-Sensing Properties of the Multiplexed Detector: The electrical performances such as transfer and output characteristics of the fabricated device were characterized by probe station (Keithley 4200-SCS). For the operation of the multiplexed detector, bias of 30, 2, and 30 V were applied to the terminals of the V_G, V_D, and $V_{photoconductor}$, respectively. To evaluate the pressure-sensing characteristics, a well-defined load was applied and measured using an experimental set-up consisting of a motorized *z*-axis stage (Mark-10 ESM303) and a force gauge (Mark-10 M7-20). For real-time imaging of spatial pressure distribution, three sourcemeters (Keithley 2400), system switch (Keithley 3706), relay card (Keithley 3723). Customized strap-type, flexible cables were connected to the source, drain, and gate electrodes of the multiplexed detector using anisotropic conducting paste. The other side of the straps was connected to the peripheral device that connected to processing modules. For applying the bias to $V_{photocondcutors}$, Cu enamel wire was connected to the top electrode (ITO) of X-ray conducting layers using the conducting paste and other side of the wire was connected to the sourcemeter (Keithley 2400). The output signal was exhibited using the Labview-based customized imaging software.

Characterization of X-Ray Sensing Properties of the Multiplexed Detector: The X-ray sensing performances of the multiplexed detector were characterized by identical conditions and set-ups with pressure-sensing performance. The target in the X-ray tube was made of tungsten and the maximum output was 16 W. The X-ray tube voltage was kept at 50 kV and the range of dose rate was from 0.2 to 3.1 $mGy_{air}\ s^{-1}$. The X-ray image of the printed circuit board was obtained by the same equipment with that of pressure distribution mapping. For imaging, X-ray tube voltage was kept at 50 kV with the dose rate of 1.6 $mGy_{air}\ s^{-1}$ for 500 ms. Since the sensing area of the multiplexed detector is 2 cm × 2 cm, the area corresponding to the white box (4 cm × 4 cm) was divided into four sections and imaged separately, then they were combined together to make a complete image.

In Vivo X-Ray Imaging and Pressure Sensing for Medical Diagnostics: All in vivo studies were conducted according to the guidelines of the National Institutes of Health for Care and Use of Laboratory Animals and with the approval of the Institute of Animal Care and Use Committee of Yonsei University (IACUC-A-202011-1164-01). A male Wistar rat was used for the in vivo imaging experiments (age: 4–6 weeks; weight: 175 g).

Supporting Information

Supporting Information is available from the Wiley Online Library or from the author.

Acknowledgements

J.J. and S.J. contributed equally to this work. This work was supported by the Ministry of Science & ICT (MSIT) and the Ministry of Trade, Industry and Energy (MOTIE) of Korea through the National Research Foundation (2019R1A2B5B03069358, 2017R1A2B3011967 and 2016R1A5A1009926), the Bio & Medical Technology Development Program (2018M3A9F1021649), the Nano Material Technology Development Program (2016M3A7B4910635), and the Technology Innovation Program (20010366 and 20013621, Center for Super Critical Material Industrial Technology). Also, the authors thank financial support by the Research Program (2019-22-0228) funded by Yonsei University.

Conflict of Interest

The authors declare no conflict of interest.

Data Availability Statement

Research data are not shared.

Keywords

lead halide perovskites, multimodal sensors, perovskites, pressure sensors, tactile sensors, X-ray detectors

Received: December 18, 2020
Revised: February 5, 2021
Published online: June 17, 2021

[1] A. J. Bandodkar, J. Choi, S. P. Lee, W. J. Jeang, P. Agyare, P. Gutruf, S. Wang, R. A. Sponenburg, J. T. Reeder, S. Schon, T. R. Ray, S. Chen, S. Mehta, S. Ruiz, J. A. Rogers, *Adv. Mater.* **2019**, *31*, 1902109.
[2] K. Sim, Z. Rao, F. Ershad, C. Yu, *Adv. Mater.* **2020**, *32*, 1902417.
[3] Y. Ai, T. H. Hsu, D. C. Wu, L. Lee, J.-H. Chen, Y.-Z. Chen, S.-C. Wu, C. Wu, Z. M. Wang, Y.-L. Chueh, *J. Mater. Chem. C* **2018**, *6*, 5514.
[4] Y. J. Yoo, W.-G. Kim, J. H. Ko, Y. J. Kim, Y. Lee, S. G. Stanciu, J.-M. Lee, S. Kim, J.-W. Oh, Y. M. Song, *Adv. Sci.* **2020**, *7*, 2000978.
[5] R. Yin, Z. Xu, M. Mei, Z. Chen, K. Wang, Y. Liu, T. Tang, M. K. Priydarshi, X. Meng, S. Zhao, B. Deng, H. Peng, Z. Liu, X. Duan, *Nat. Commun.* **2018**, *9*, 2334.
[6] Y.-G. Park, S. Lee, J.-U. Park, *Sensors* **2019**, *19*, 4353.
[7] S. Ji, J. Jang, E. Cho, S.-H. Kim, E.-S. Kang, J. Kim, H.-K. Kim, H. Kong, S.-K. Kim, J.-Y. Kim, J.-U. Park, *Adv. Mater.* **2017**, *29*, 1700538.

[8] J. Jang, B. Oh, S. Jo, S. Park, H. S. An, S. Lee, W. H. Cheong, S. Yoo, J.-U. Park, *Adv. Mater. Technol.* **2019**, *4*, 1900082.
[9] J. Jang, H. Kim, S. Ji, H. J. Kim, M. S. Kang, T. S. Kim, J. Won, J.-H. Lee, J. Cheon, K. Kang, W. B. Im, J.-U. Park, *Nano Lett.* **2020**, *20*, 66.
[10] R. Gautier, F. Massuyeau, G. Galnon, M. Paris, *Adv. Mater.* **2019**, *31*, 1807383.
[11] Y. Huang, Y. Feng, F. Li, F. Lin, Y. Wang, X. Chen, R. Xie, *TrAC, Trends Anal. Chem.* **2021**, *134*, 116127.
[12] N.-H. Yang, Y.-F. Song, R.-S. Liu, *ACS Energy Lett.* **2018**, *3*, 1911.
[13] Q. Chen, J. Wu, X. Ou, B. Huang, J. Almutlaq, A. A. Zhumekenov, X. Guan, S. Han, L. Liang, Z. Yi, J. Li, X. Xie, Y. Wang, Y. Li, D. Fan, D. B. L. Teh, A. H. All, O. F. Mohammed, O. M. Bakr, T. Wu, M. Bettinelli, H. Yang, W. Huang, X. Liu, *Nature* **2018**, *561*, 88.
[14] Y. C. Kim, K. H. Kim, D.-Y. Son, D.-N. Jeong, J.-Y. Seo, Y. S. Choi, I. T. Han, S. Y. Lee, N.-G. Park, *Nature* **2017**, *550*, 87.
[15] M. J. Yaffe, J. A. Rowlands, *Phys. Med. Biol.* **1997**, *42*, 1.
[16] H. U. Chung, B. H. Kim, J. Y. Lee, J. Lee, Z. Xie, E. M. Ibler, K. Lee, A. Banks, J. Y. Jeong, J. Kim, C. Ogle, D. Grande, Y. Yu, H. Jang, P. Assem, D. Ryu, J. W. Kwak, M. Namkoong, J. B. Park, Y. Lee, D. H. Kim, A. Ryu, J. Jeong, K. You, B. Ji, Z. Liu, Q. Huo, X. Feng, Y. Deng, Y. Xu, K.-I. Jang, J. Kim, Y. Zhang, R. Ghaffari, C. M. Rand, M. Schau, A. Hamvas, D. E. Weese-Mayer, Y. Huang, S. M. Lee, C. H. Lee, N. R. Shanbhag, A. S. Paller, S. Xu, J. A. Rogers, *Science* **2019**, *363*, eaau0780.
[17] S. O. Kasap, J. A. Rowlands, *J. Mater. Sci.: Mater. Electron.* **2000**, *11*, 179.
[18] C.-L. Dai, Y.-W. Tai, P.-H. Kao, *Sensors* **2007**, *7*, 3386.
[19] V. Jain, V. P. Mathur, A. Kumar, *Acta Odontol. Scand.* **2013**, *71*, 96.
[20] C. M. Capobianco, *Clin. Podiatr. Med. Surg.* **2017**, *34*, 33.
[21] H. Cho, S.-H. Jeong, M.-H. Park, Y.-H. Kim, C. Wolf, C.-L. Lee, J. H. Heo, A. Sadhanala, N. Myoung, S. Yoo, S. H. Im, R. H. Friend, T.-W. Lee, *Science* **2015**, *350*, 1222.
[22] J. Liu, B. Shabbir, C. Wang, T. Wan, Q. Ou, P. Yu, A. Tadich, X. Jiao, D. Chu, D. Qi, D. Li, R. Kan, Y. Huang, Y. Dong, J. Jasieniak, Y. Zhang, Q. Bao, *Adv. Mater.* **2019**, *31*, 1901644.
[23] H. M. Thirimanne, K. D. G. I. Jayawardena, A. J. Parnell, R. M. I. Bandara, A. Karalasingam, S. Pani, J. E. Huerdler, D. G. Lidzey, S. F. Tedde, A. Nisbet, C. A. Mills, S. R. P. Silva, *Nat. Commun.* **2018**, *9*, 2926.
[24] S. Lee, S.-W. Kim, M. Ghidelli, H. S. An, J. Jang, A. L. Bassi, S.-Y. Lee, J.-U. Park, *Nano Lett.* **2020**, *20*, 4872.
[25] J. Jang, J. Jang, H. Kim, H. Kim, Y. M. Song, J.-U. Park, J.-U. Park, *Opt. Mater. Express* **2019**, *9*, 3878.
[26] Y.-G. Park, E. Cha, H. S. An, K.-P. Lee, M. H. Song, H. K. Kim, J.-U. Park, *Nano Res.* **2020**, *13*, 1347.
[27] S. O. Kasap, J. A. Rowlands, *IEE Proc., Part G: Circuits, Devices and Systems* **2002**, *149*, 85.
[28] M. Choquette, H. Rougeot, J.-P. Martin, L. Laperriere, Z. Shukri, B. T. Polischuk, in *Medical Imaging 2000: Physics of Medical Imaging*, (Eds: J. T. Dobbins III, J. M. Boone), International Society For Optics And Photonics, Washington D.C., USA **2000**, p. 128.
[29] G. Zentai, L. D. Partain, R. Pavlyuchkova, C. Proano, G. F. Virshup, B. N. Breen, A. I. Vilensky, O. Dagan, E. Meerson, M. Schieber, H. Gilboa, J. A. Thomas, in *Smart Nondestructive Evaluation and Health Monitoring of Structural and Biological Systems II*, (Ed: T. Kundu), International Society For Optics And Photonics, Washington D.C., USA **2003**, pp. 84–95.
[30] M. M. Lee, J. Teuscher, T. Miyasaka, T. N. Murakami, H. J. Snaith, *Science* **2012**, *338*, 643.
[31] M. Abdi-Jalebi, Z. Andaji-Garmaroudi, S. Cacovich, C. Stavrakas, B. Philippe, J. M. Richter, M. Alsari, E. P. Booker, E. M. Hutter, A. J. Pearson, S. Lilliu, T. J. Savenije, H. Rensmo, G. Divitini, C. Ducati, R. H. Friend, S. D. Stranks, *Nature* **2018**, *555*, 497.
[32] M. Saliba, T. Matsui, J.-Y. Seo, K. Domanski, J.-P. Correa-Baena, M. Khaja Nazeeruddin, S. M. Zakeeruddin, W. Tress, A. Abate, A. Hagfeldt, M. Grätzel, *Energy Environ. Sci.* **2016**, *9*, 1989.
[33] A. D. Jodlowski, C. Roldán-Carmona, G. Grancini, M. Salado, M. Ralaiarisoa, S. Ahmad, N. Koch, L. Camacho, G. de Miguel, M. K. Nazeeruddin, *Nat. Energy* **2017**, *2*, 972.
[34] D. J. Kubicki, D. Prochowicz, A. Hofstetter, M. Saski, P. Yadav, D. Bi, N. Pellet, J. Lewiński, S. M. Zakeeruddin, M. Grätzel, L. Emsley, *J. Am. Chem. Soc.* **2018**, *140*, 3345.
[35] Y. Xu, J. Duan, X. Yang, J. Du, Y. Wang, Y. Duan, Q. Tang, *J. Mater. Chem. A* **2020**, *8*, 11859.
[36] A. J. Neukirch, W. Nie, J.-C. Blancon, K. Appavoo, H. Tsai, M. Y. Sfeir, C. Katan, L. Pedesseau, J. Even, J. J. Crochet, G. Gupta, A. D. Mohite, S. Tretiak, *Nano Lett.* **2016**, *16*, 3809.
[37] N. De Marco, H. Zhou, Q. Chen, P. Sun, Z. Liu, L. Meng, E.-P. Yao, Y. Liu, A. Schiffer, Y. Yang, *Nano Lett.* **2016**, *16*, 1009.
[38] A. Pisoni, J. Jaćimović, O. S. Barišić, M. Spina, R. Gaál, L. Forró, E. Horváth, *J. Phys. Chem. Lett.* **2014**, *5*, 2488.
[39] E. Vega, M. Mollar, B. Marí, *J. Alloys Compd.* **2018**, *739*, 1059.
[40] K. Nomura, H. Ohta, A. Takagi, T. Kamiya, M. Hirano, H. Hosono, *Nature* **2004**, *432*, 488.
[41] S.-H. Shin, S. Ji, S. Choi, K.-H. Pyo, B. Wan An, J. Park, J. Kim, J.-Y. Kim, K.-S. Lee, S.-Y. Kwon, J. Heo, B.-G. Park, J.-U. Park, *Nat. Commun.* **2017**, *8*, 14950.
[42] S. Ji, J. Jang, J. C. Hwang, Y. Lee, J.-H. Lee, J.-U. Park, *Adv. Mater. Technol.* **2020**, *5*, 1900928.
[43] J. Jang, Y. S. Jun, H. Seo, M. Kim, J.-U. Park, *Sensors* **2020**, *20*, 3624.
[44] W. H. Cheong, B. Oh, S.-H. Kim, J. Jang, S. Ji, S. Lee, J. Cheon, S. Yoo, S.-Y. Lee, J.-U. Park, *Nano Energy* **2019**, *62*, 230.
[45] J. H. Park, S. C. Noh, H. S. Jang, W. J. Yu, M. K. Park, H. H. Choi, in *13th Int. Conf. Biomedical Engineering*, (Eds: C. T. Lim, J. C. H. Goh), Springer, Berlin/Heidelberg, Germany **2009**, pp. 974–978.
[46] Y. Narukawa, N. Ooka, Z. Makihara, Y. Nemoto, K. Yokota, in *15th Asia Pacific Conf. for Non-Destructive Testing*, Singapore, **2018**, p. 8.